九州大学学術情報リポジトリ
Kyushu University Institutional Repository

Effects of sea surface temperature anomalies on heavy rainfall in Tsushima Strait in late July 2020

Yamamoto, Masaru
Research Institute for Applied Mechanics, Kyushu University

https://hdl.handle.net/2324/7160878

出版情報：Atmospheric Research. 278, pp.106336-, 2022-11. Elsevier
バージョン：
権利関係：© 2022 The Author.

KYUSHU UNIVERSITY

Atmospheric Research 278 (2022) 106336

Contents lists available at ScienceDirect

Atmospheric Research

journal homepage: www.elsevier.com/locate/atmosres

Effects of sea surface temperature anomalies on heavy rainfall in Tsushima Strait in late July 2020

Masaru Yamamoto *

Research Institute for Applied Mechanics, Kyushu University, Kasuga, Fukuoka 816-8580, Japan

ARTICLE INFO

Keywords:
Heavy rainfall
Sea surface temperature
East-Asian marginal seas

ABSTRACT

Short-period responses of moisture and precipitation to sea surface temperature (SST) are investigated in model simulations for the case of heavy precipitation in the Tsushima Strait on 26 July 2020, where both atmospheric and oceanic fronts were established and SST was much lower than the climatological normal (30-year average in late July) in the vicinity of the strait. Compared with the experiments using the climatological normal SST, the surface latent heat flux and water vapor are lower (higher) in the cooler Tsushima Strait (warmer southern East China Sea) in the control experiment. The area-mean precipitation is lowered by the reduced moisture supply over the cooler adjacent sea in the Tsushima Strait. The heavy rainfall is enhanced in the strait via the transport and convergence of remote moisture from the East China Sea. The ensemble-mean maximum rainfall in the strait is higher than that using the climatological normal SST, whereas the maxima are lower over land because of the northward shift of the precipitation area caused by the cool SST anomaly. Although the strong surface baroclinicity over the SST front in the Tsushima Strait and the remote sea surface conditions over the southern East China Sea do not directly influence heavy rainfall, the SST anomaly in the vicinity of the strait influences it. The intensity and area of heavy rainfalls potentially leading to natural disasters are sensitive to large SST anomalies in the marginal seas adjacent to highly populated cities near the coast. In this case, when there is a local negative SST anomaly, the area of heavy precipitation shifts away from land, reducing the rainfall over populated areas.

1. Introduction

Heavy precipitation due to quasi-stationary convective systems has often been observed in the rainy season of the northern Kyushu Island (K in Fig. 1b; e.g., Kato et al., 2018; Kawano and Kawamura, 2020; Nayak and Takemi, 2021; Ito et al., 2021). A stationary atmospheric front is located in the late rainy season (late July) in the Tsushima Strait between the Kyushu Island and the Korean Peninsula (KP in Fig. 1b), which links the eastern Chinese marginal seas (Yellow and East China Seas, Y and E in Fig. 1a) and the Sea of Japan (J in Fig. 1a) via oceanic flows and the along-strait winds (Takikawa et al., 2005; Isoguchi and Kawamura, 2007; Shimada, 2010). It is not fully understood how the sea surface conditions influence heavy rainfall associated with the quasi-stationary atmospheric front over the strait in the late rainy season.

The responses of precipitation to sea surface temperature (SST) have been widely investigated for various oceanic areas (e.g., Pastor et al., 2015; Cassola et al., 2016; Ferrari et al., 2020). In the case of torrential rainfall events in summer in Japan, warm SST was found to induce extremely high precipitation (Manda et al., 2014). For a humid air flow over the southern coast of Japan from Tropical Cyclone Talas in 2011, the coastal warm SST anomaly enhanced the surface latent heat flux via the positive feedback of the amplified surface-horizontal winds and influenced the precipitation pattern (Yamamoto, 2014). Iizuka and Nakamura (2019) reported that warm SSTs over the Sea of Japan led to an increase in 24-h precipitation averaged over the northern Tohoku region on 9 August 2013. Yamamoto (2020) focused on the mesoscale warm SST in the Tsushima Strait and its related water vapor, which locally induced heavy rainfall in August 2013 over the sea area.

The influence of SST fronts on precipitation has been examined previously (e.g., Minobe et al., 2008; Kuwano-Yoshida et al., 2010; Miyama et al., 2012; Toy and Johnson, 2014). However, it remains unclear whether the development of the SST front (surface high baroclinicity) influences short-term (24-h) precipitation over the Tsushima Strait in the late rainy season. In addition to SST in the vicinity of the precipitation area, the atmospheric transport of large amounts of moisture from the south is a major cause of floods and torrential rainfall over western Japan (Manda et al., 2014; Nayak and Takemi, 2021; Zhao et al., 2021). In these cases, large amounts of moisture are supplied over

* Corresponding author.
E-mail address: yamakatu@kyudai.jp.

https://doi.org/10.1016/j.atmosres.2022.106336
Received 3 December 2021; Received in revised form 23 May 2022; Accepted 4 July 2022
Available online 6 July 2022
0169-8095/© 2022 The Author. Published by Elsevier B.V. This is an open access article under the CC BY license (http://creativecommons.org/licenses/by/4.0/).

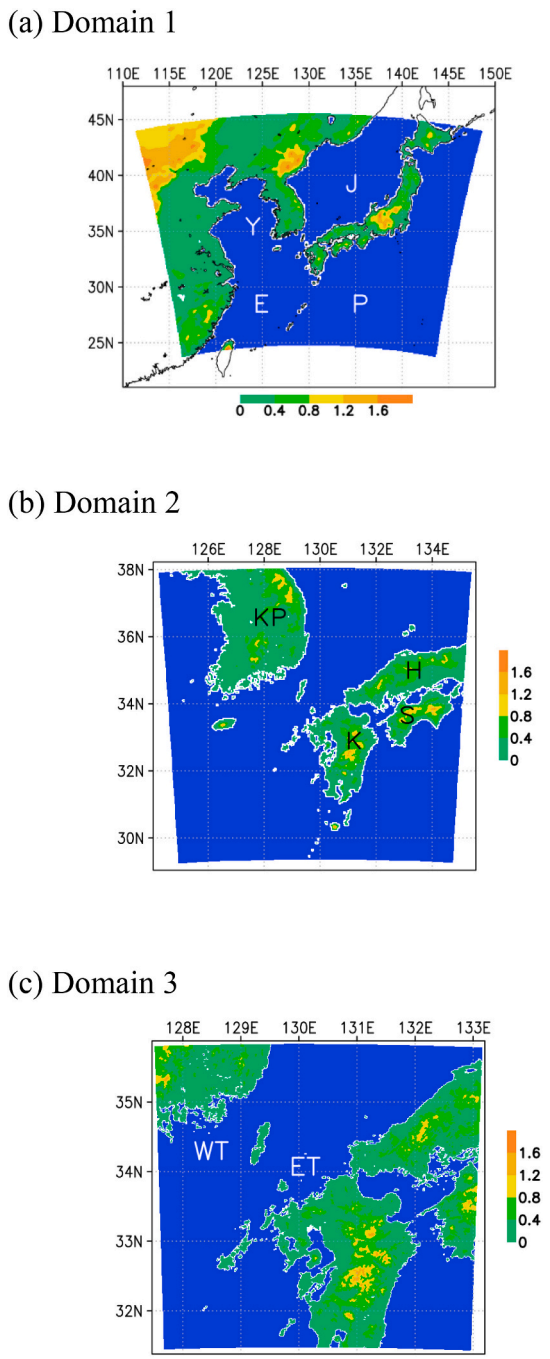

Fig. 1. (a–c) Areas of model domains 1 to 3, along with terrain height (km, shading), sea area (blue), and locations of the Sea of Japan (J), Yellow Sea (Y), East China Sea (E), Philippine Sea (P), Korean Peninsula (KP), Kyushu Island (K), Shikoku Island (S), Honshu Island (H), Western Channel of the Tsushima Strait (WT), and Eastern Channel of the Tsushima Strait (ET). (For interpretation of the references to color in this figure legend, the reader is referred to the web version of this article.)

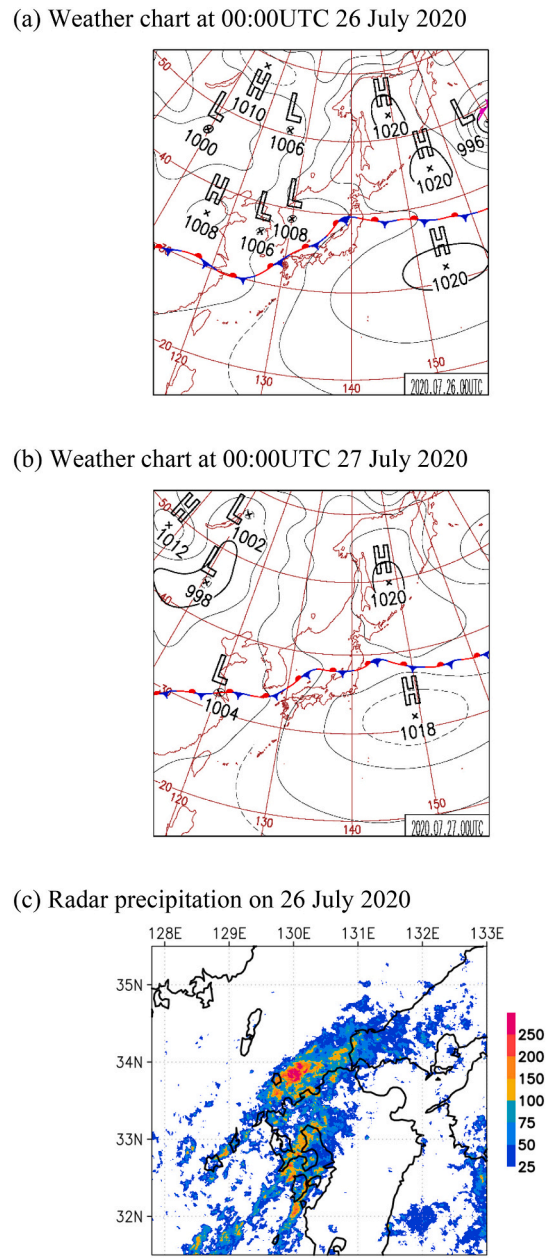

Fig. 2. Meteorological data of Japan Meteorological Agency. Surface weather charts in Japan at 0000 UTC (a) 26 July 2020 and (b) 27 July 2020. (c) Daily radar precipitation (mm) on 26 July 2020.

the remote oceans and transported toward the atmospheric front. Thus we need to consider the impacts of both the remote and adjacent seas on heavy rainfall associated with the stationary atmospheric front.

Record-breaking heavy precipitation hit the Japanese islands and led to flooding and extreme damage in July 2020. In the Tsushima Strait, both the atmospheric front and the SST front were established in the late July. On 26 July 2020, the stationary atmospheric front was located over the Tsushima Strait (Fig. 2a and b), where the horizontal SST gradient was high (contours in Fig. 3a–c). Precipitation radar data show heavy precipitation of >200 mm/day (Fig. 2c) over the Eastern Channel of the Tsushima Strait (ET in Fig. 1c).

In general, sea-surface condition varies on seasonal timescales in the Yellow Sea (Moteki and Manda, 2013) during rainy season between spring and summer. Associated with the time lag of the seasonal SST warming, the SST anomaly with respect to the climatological normal (30-year average in late July) appears in the shallow marginal seas. According to Japan Meteorological Agency/High resolution Merged

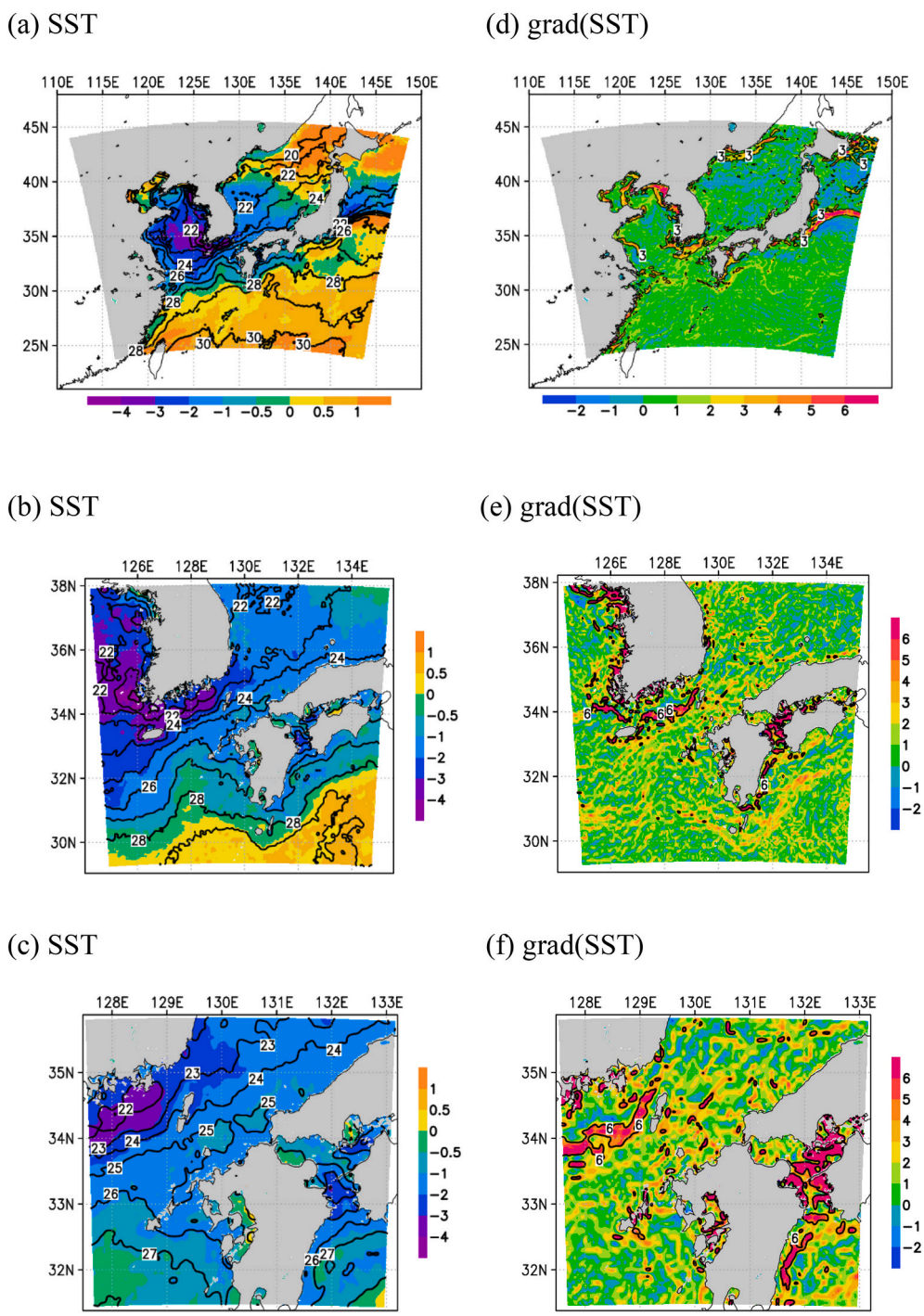

Fig. 3. Distributions of (a–c) SST (K, contours) and (d–f) gradient of SST (K deg.$^{-1}$, contours) in CNTL and their differences from CLIM (CNTL − CLIM, color shading) in (a, d) Domain 1, (b, e) Domain 2 and (c, f) Domain 3.

satellite and in situ data Sea Surface Temperature (JMA/HIMSST), the SST in late July 2020 was cooler than the climatological normal in the Yellow Sea, northern East China Sea, and Tsushima Strait (negative in Fig. 3a), whereas it was warmer in the southern East China Sea and Philippine Sea (positive in Fig. 3a). In particular, the cool (negative) SST anomaly was large (>3 K) in the Yellow Sea, though the warm (positive) SST anomaly was weak (<1 K) in the southern East China and Philippine Seas. Such a large SST anomaly may modify the intensity and area of the precipitation over the marginal seas. Compared with the climatological normal, the large-scale temperature contrast between the cool Yellow Sea and the warm southern East China Sea was enhanced (Fig. 3a), with local, strong SST gradients in the coastal areas of the Korean Peninsula (Fig. 3d–f).

In this article, the atmospheric response to the large SST anomaly with respect to the climatological normal in the Tsushima Strait is investigated for the case of heavy precipitation on 26 July 2020 in short-term (24-h) simulations (Section 2). The analysis focuses on heavy rainfall and its related moisture (Section 3). Finally, the results are summarized and discussed in Section 4.

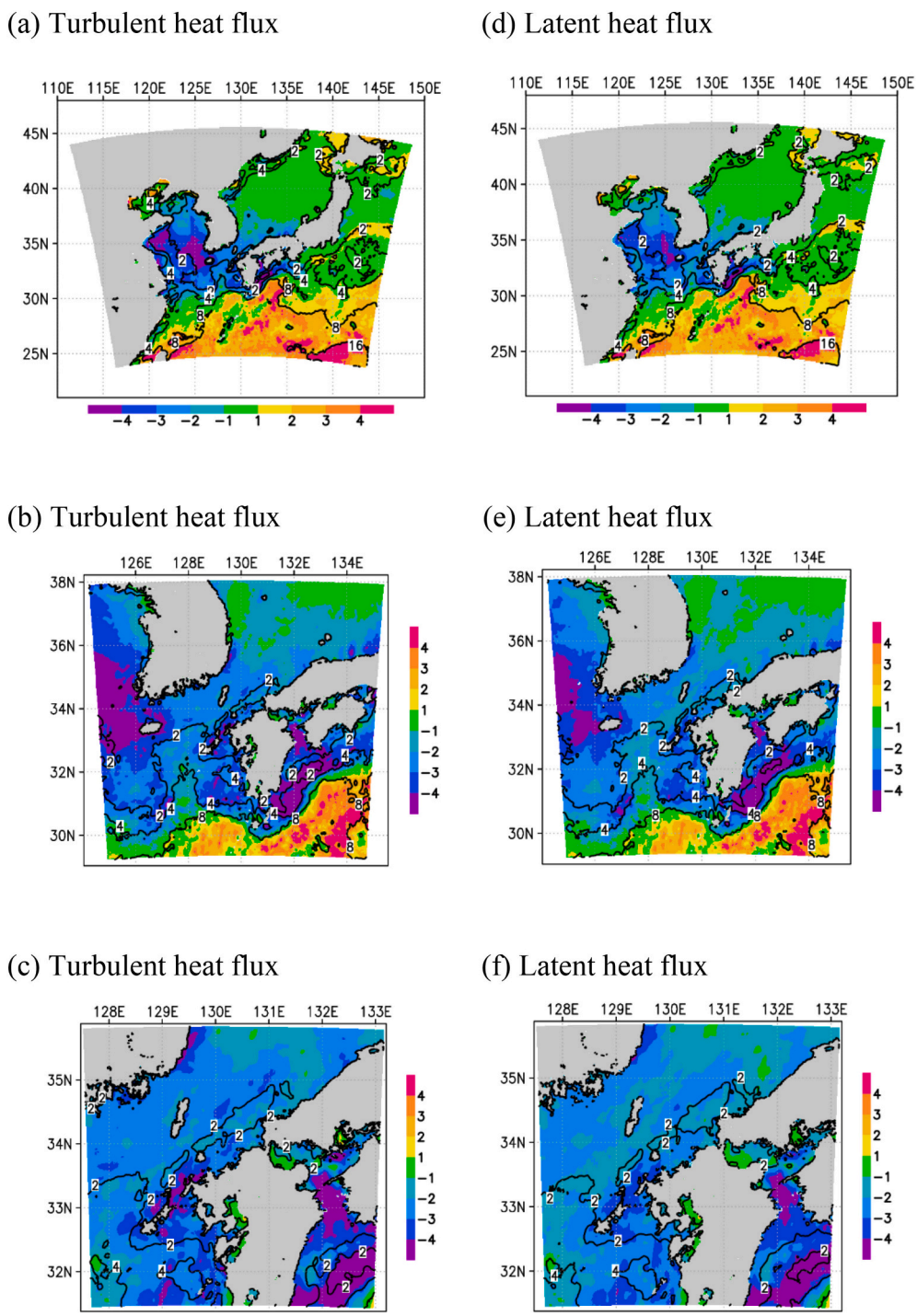

Fig. 4. Distributions of differences in accumulated upward (a–c) turbulent and (d–f) latent heat fluxes at the surface on 26 July 2020 (MJ m^{-2}, contours) between CNTL and CLIM (CNTL − CLIM, color shading) in (a, d) Domain 1, (b, e) Domain 2 and (c, f) Domain 3. The contours indicate the sea-surface fluxes in CNTL.

2. Data and model

Nested simulations using the Advanced Research Weather Research and Forecasting model (WRF–ARW, ver. 4.2; Skamarock et al., 2008) were employed to investigate the influence of SST on rainfall in the Tsushima Strait during 26 July 2020. The atmosphere between the surface and the 50-hPa level is divided into 40 eta levels defined in a terrain-following hydrostatic-pressure vertical coordinate. Domain 1 (the parent domain, Fig. 1a) on a 181 × 145 grid with a horizontal grid spacing of 16 km is centered on 130°E, 35°*N*. Domain 2 (the second domain, Fig. 1b) on a 241 × 241 grid with a horizontal grid spacing of 4 km starts from the point $I = 60$ and J = 34 of Domain 1 (where I and J are

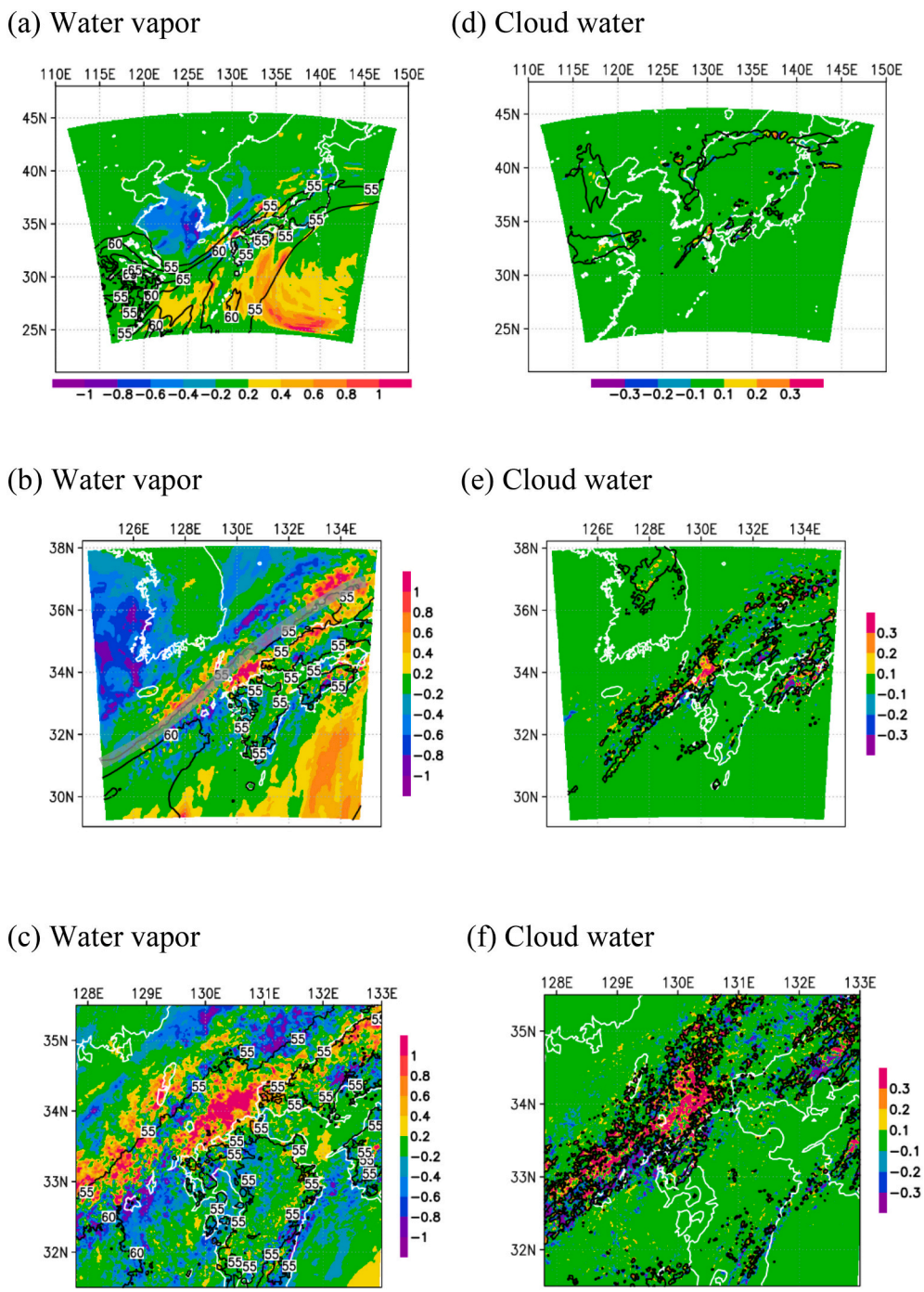

Fig. 5. Distributions of differences in vertically integrated (a–c) vapor and (d–f) cloud water from 1000 hPa to 100 hPa on 26 July 2020 (mm, contours) between CNTL and CLIM (CNTL − CLIM, color shading) in (a, d) Domain 1, (b, e) Domain 2 and (c, f) Domain 3. The contours indicate the vertically integrated amounts in CNTL. The contours in (d–f) represent 0.3 mm of vertically integrated cloud water.

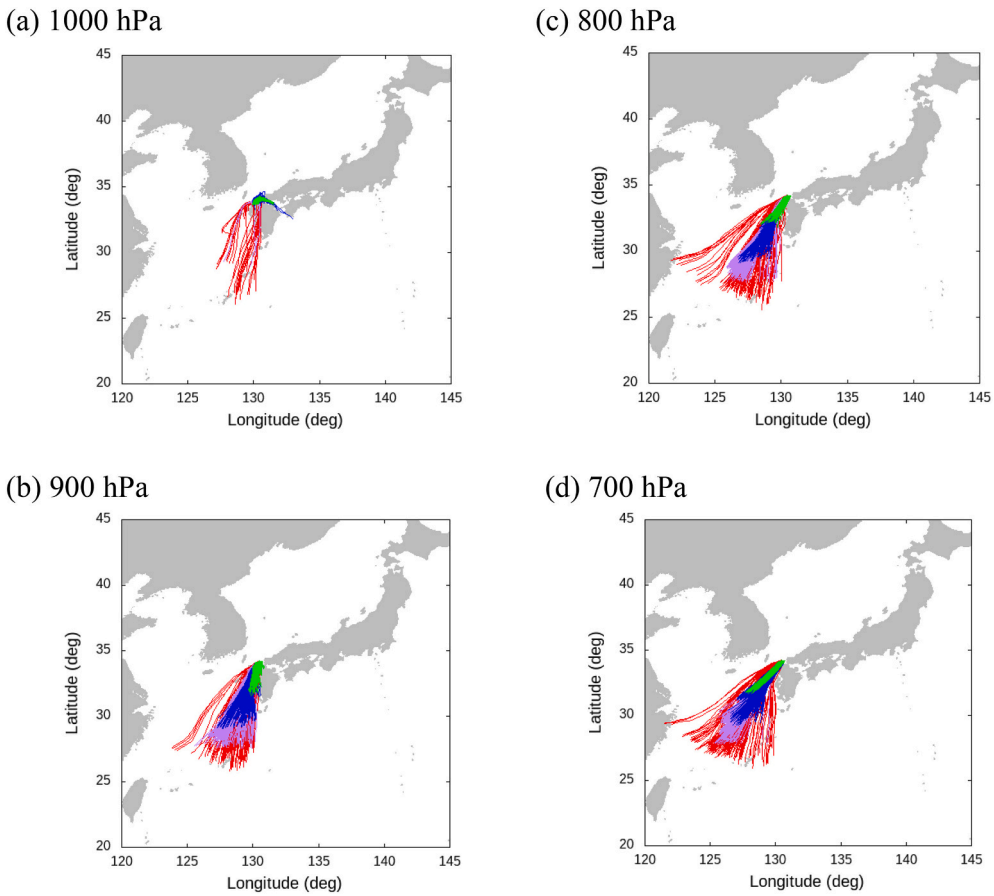

Fig. 6. Longitude–latitude cross-sections of backward trajectories of air parcels initially located at (a) 1000, (b) 900, (c) 800, and (d) 700 hPa in the area of the large difference in vertically integrated vapor between CLIM and CNTL. The backward trajectory started each hour on 26 July 2020 (T_{INIT}) and ended at 0000 UTC on 26 July 2020. T_{INIT} = 1–6 h (green), 7–12 h (blue), 13–18 h (purple), and 19–24 h (red) on 26 July 2020. (For interpretation of the references to color in this figure legend, the reader is referred to the web version of this article.)

the west-to-east grid number and south-to-north grid number counted from the southwest corner of the outer domain, respectively), and covers South Korea and western Japan. Domain 3 (the third domain, Fig. 1c) on a 501 × 481 grid with a horizontal grid spacing of 1 km starts from the point $I = 70$ and J = 60 of Domain 2, and covers the Tsushima Strait. The meteorological elements of these domains interact by two-way nesting. The following physics options are used: the microphysics scheme of Thompson et al. (2008), the cumulus scheme of Tiedtke (1989), the Rapid Radiative Transfer Model for GCMs (Iacono et al., 2008), the planetary-boundary layer scheme of Mellor–Yamada–Janjic (Janjic, 1994), the Eta surface layer scheme (Janjic, 1996, 2002), and the Noah Land Surface Model (Chen and Dudhia, 2001). Cumulus parameterization is not applied to Domains 2 and 3 because it should not be used for resolution of <5 km (Skamarock et al., 2008).

The National Centers for Environmental Prediction/Final (NCEP/FNL, ds083.3) analyses dataset and JMA/HIMSST were used for the initial and boundary conditions. The SST in the Western North Pacific in late July 2020 (contours of Fig. 3a–c) was used for a control experiment (CNTL). The climatological normal SST was used for a comparative experiment (CLIM). The SST difference between CLIM and CNTL is shown in Fig. 3a–c (shading). The present study investigates the influence of the SST difference on short-term heavy rainfall in the presence of the SST front in the Tsushima Strait.

The simulation was performed from 0000 UTC 25 July 2020 to 0000 UTC 27 July 2020 (Run +00 in Table S1–S4). 3D-grid nudging of wind, temperature, and water vapor was applied to Domain 1 during the spin-up period before 0000 UTC on 26 July to reproduce the appropriate distributions of wind, temperature, and water vapor in the coarser domain. After the spin-up, the nudging-free run was conducted for the analysis period (from 0000 to 2400 UTC 26 July). Ensemble experiments were conducted in this study to check the sensitivity to the spin-up, of which initial times are listed in Table S1–S4. In the ensemble experiments in CNTL and CLIM, the nudging was applied to Domain 1 during the spin-up (from the initial time of the simulation to 0000 UTC 26 July 2020) using the sea surface condition in late July 2020 (contours in Fig. 3a–c). During 26 July 2020 (from 0000 UTC 26 to 0000 UTC 27 July 2020), SST in late July 2020 was used in CNTL and the climatological normal was used in CLIM. Because the atmospheric conditions are the same between CNTL and CLIM at the initial time of the analyses (0000 UTC 26 July 2020) for each ensemble run, the simulated difference between the two experiments is caused by the SST difference during 26 July 2020.

As shown in Table S1-S4, the initial time of Run +00 is around the center of the ensemble spread of the initial time. The results in Run +00 are analyzed in Section 3, as the maximum daily precipitation (273 mm) is almost the same as the ensemble average (289 mm) in the Tsushima Strait (Table S3) (the difference from the ensemble average (16 mm) is the smallest in the ensemble members). Differences between the ensemble members are also discussed, based on the supplementary material.

To overview the meteorological conditions and validate the model output, the present study used JMA weather charts and radar echo intensity data on a 1 km × 1 km resolution grid over Japan. In addition, the present work also used an operational objective analysis dataset for

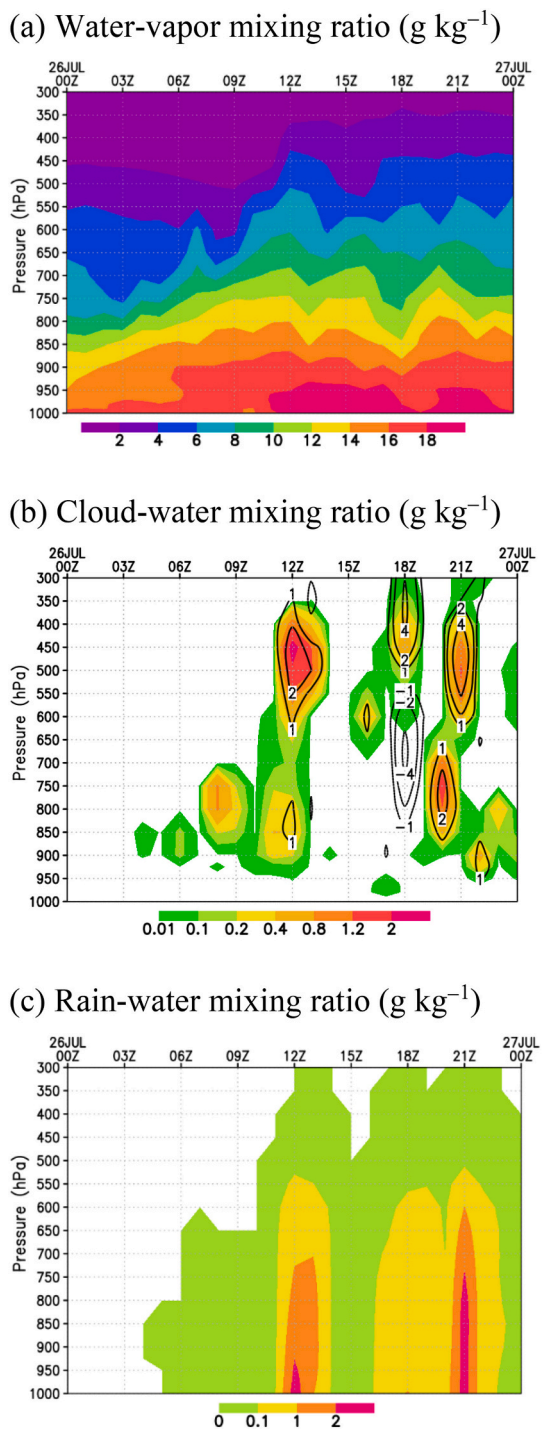

Fig. 7. Time–pressure cross-sections of (a) water–vapor mixing ratio (g kg^{-1}), (b) cloud–water mixing ratio (g kg^{-1}), and (c) rain–water mixing ratio (g kg^{-1}) at the location of the daily precipitation maximum in run +00 of CNTL (color shading), along with the vertical flow (m s^{-1}, contours) in panel b.

initial data of the JMA meso-scale model (MSM) with 5 km grid spacing and a columnar water vapor estimated from the Advanced Microwave Scanning Radiometer 2 (AMSR2, Wentz et al., 2014) in the supplementary material.

Backward trajectory analysis based on Stunder (1996) was also conducted (Appendix C in Yamamoto, 2018). The air parcels are initially located at 1000–700 hPa in the area of large difference of vertically integrated vapor between CLIM and CNTL (|CLIM − CNTL| > 1 mm). The backward trajectories start each hour on 26 July 2020 (T_{INIT}) and end at 0000 UTC 25 July 2020.

3. Results

Before investigating comparative experiments in CNTL and CLIM, the CNTL simulation is overviewed here using the meteorological elements (wind, air temperature, and relative humidity). The surface wind and sea-level pressure in CNTL are similar to the objective analysis data for the MSM, though the simulated relative humidity is somewhat higher over the seas where weather observation data of relative humidity are insufficient (Fig. S1). At the 700-hPa level, the meteorological elements in Run +00 of CNTL are similar to the objective analysis data for the MSM (Fig. S2). The humid flow over Japan is seen in the objective analysis data and CNTL simulation. Such an atmospheric river stayed during 26 July 2020 in the AMSR2 columnar water vapor map (Fig. S3). The columnar water vapor of >55 mm is simulated in Section 3.2. Heavy precipitation of >200 mm/day (Fig. 2c) was located over the Eastern Channel of the Tsushima Strait in the JMA radar precipitation. Such a heavy rainfall is also simulated in CNTL (Section 3.4). Accordingly, it is considered that the CNTL simulation reproduced the meteorological condition in and around the Tsushima Strait on 26 July 2020. Based on the comparisons between the CNTL and CLIM, meteorological impacts of the SST anomaly are discussed in the following subsections.

3.1. Distributions of surface heat fluxes

Fig. 4 shows the horizontal distributions of accumulated surface turbulent and latent heat fluxes over 26 July 2020 in CNTL (contours), together with the difference in these fluxes between CNTL and CLIM (color shading). The surface turbulent heat flux (the surface flux of latent heat plus sensible heat) is ~2 MJ m^{-2} in the Yellow Sea and the Sea of Japan and > 8 MJ m^{-2} over the Philippine and southern East China Seas. Because the surface sensible heat flux is very small in the seas around Japan, the distribution of latent heat flux is almost the same as that of turbulent heat flux. Compared with CLIM, the surface latent heat fluxes in CNTL are weaker in the cooler Yellow and northern East China Seas (>30°N, blue in Fig. 4d) and enhanced in the warmer Philippine and southern East China Seas (<30°N, orange in Fig. 4d). The supply of water vapor from the Tsushima Strait in CNTL is smaller than that in CLIM: the difference in the surface latent heat flux is negative (blue in Fig. 4e and f) over the negative SST anomaly area (blue in Fig. 3b and c).

3.2. Distributions of water vapor and cloud water

A tongue-shaped area of high vertically integrated water vapor (>55 mm contours in Fig. 5a) extends from southern China and the East China Sea to western Japan. Such a moist tongue was also observed in the AMSR2 measurement (Fig. S3) and corresponds to the humid air flow at 700 hPa over Japan in the JMA MSM objective analysis data (Fig. S2). The difference in water vapor north of the tongue-shaped moist area is negative (blue in Fig. 5a) over the negative SST anomaly area, whereas the difference in the southern moist area is positive (<30°N; yellow in Fig. 5a) over the positive SST anomaly area. The positive and negative

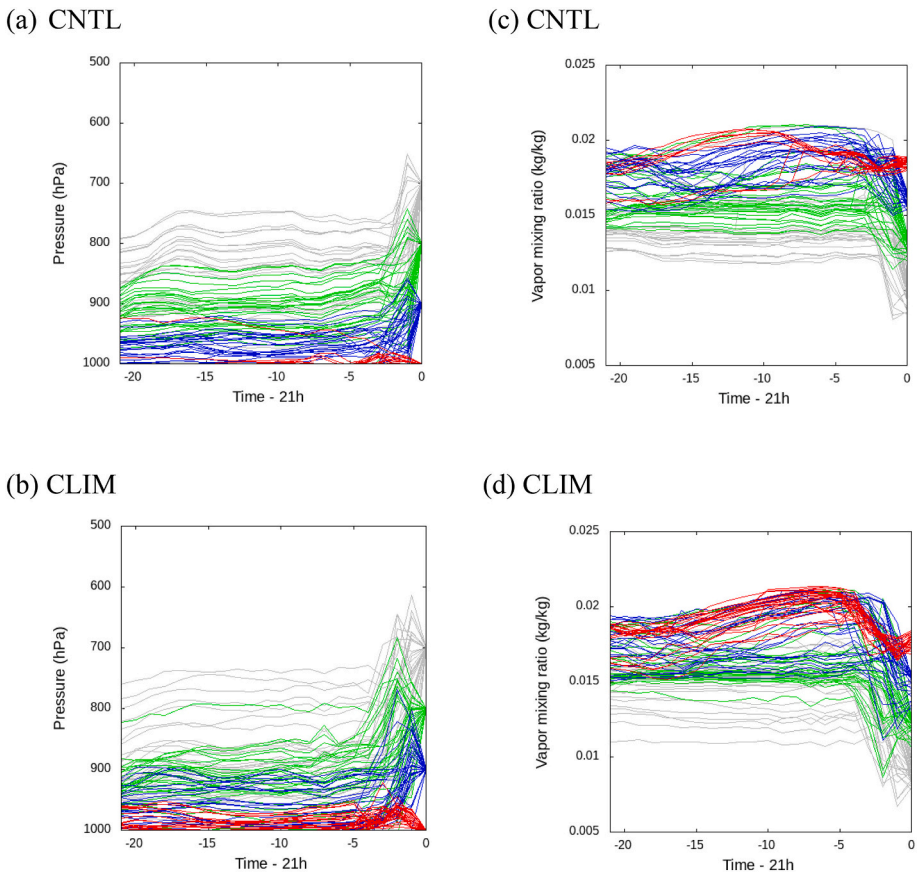

Fig. 8. (a, b) Time–pressure cross-sections of backward trajectories of air parcels initially located at 1000 (red), 900 (blue), 800 (green), and 700 hPa (gray) in the area of large difference between CNTL and CLIM of vertically integrated vapor (CNTL − CLIM >1 mm), together with (c, d) the water vapor mixing ratio (kg $^{-1}$), in (a, b) CNTL and (c, d) CLIM. Units of time and pressure are h and hPa, respectively. The backward trajectory started from 2100 UTC on 26 July 2020 (0 h) and ended at 0000 UTC 26 July 2020 (−21*h*). (For interpretation of the references to color in this figure legend, the reader is referred to the web version of this article.)

differences in the water vapor are associated with the differences in the upward surface moisture supply (surface latent heat flux) from the adjacent seas. At the northern edge of the tongue-shaped region over the Kyushu (atmospheric front, a gray transparent line of Fig. 5b), localized patches of positive moisture difference also appear (red in ~34°N, ~130°E in Fig. 5b and c), although the difference in the surface moisture supply is negative.

High values of vertically integrated cloud water are located along the front (the northern edge of the moist tongue) in the Tsushima Strait for CNTL (Fig. 5d and e). In the cloud-free or hazy-cloud region outside the front, the difference in water vapor does not greatly influence the amount of cloud water because a large amount of the vapor does not condense. Thus the difference in cloud water is apparent in the vicinity of the linear cloud band along the front. Compared with CLIM, the cloud water increases in the frontal cloud region in CNTL (red in Fig. 5d–f), whereas it decreases (blue and purple in Fig. 5d–f) in the southern area of the cloud band where the vertically integrated cloud water is >0.3 mm in Fig. 5e and f. The enhanced water vapor (CNTL − CLIM >0) increases the cloud water in the vicinity of the front.

The tongue-shaped moist area and linear cloud band are simulated north of Kyushu Island in the ensemble experiment (contours in Figs. S4 and S5), although there are some differences between the ensemble members. In the Eastern Channel of the Tsushima Strait, the large differences in water vapor and cloud water between CNTL and CLIM are also simulated in all the ensemble members (gray circles in Figs. S4 and S5). Thus, the characteristics of water vapor and clouds in Figs. 4 and 5 (the tongue-shaped moist area, linear cloud band, and moisture responses to the SST anomaly in late July 2020) are robust.

3.3. Horizontal transport of water vapor

As mentioned above, the vapor is locally enhanced along the northern edge of the moist region (corresponding to the stationary atmospheric front of the vapor) over the Eastern Channel of the Tsushima Strait (~34.0°N, ~130.5°E in Fig. 5c), north of Kyushu Island. Air parcels located in the area of large water-vapor difference (>1 mm) are advected from the southern East China Sea (Fig. 6), where the SST and surface vapor (latent heat) flux in CNTL are greater than those in CLIM (CNTL − CLIM >0). This indicates that moisture transport from the remote southern seas locally increases the water vapor in the vicinity of the atmospheric front.

At the location of the daily precipitation maximum in run +00 of CNTL, the mixing ratio of water vapor is higher than ~10 g kg^{-1} in the lower-level atmosphere below the 700-hPa altitude after 12 h and 16–18 g kg^{-1} at 1000 hPa in Fig. 7a. The rain–water mixing ratio is enhanced around 1200 and 2100 UTC (Fig. 7c) at the location of the daily mean precipitation maximum, associated with strong vertical flows and convective clouds (Fig. 7b). Abundant moisture leading to heavy rainfall is transported from the southern East China Sea area (Fig. 6) and converges into the frontal area where the vertically integrated vapor in CNTL is higher than that in CLIM (red in Fig. 5c).

For the backward trajectories from the rainfall event at 2100 UTC, the parcels below 700-hPa rose in the 1–3 h before the rainfall event (Fig. 8a), and the water vapor transformed into cloud or rain (the vapor

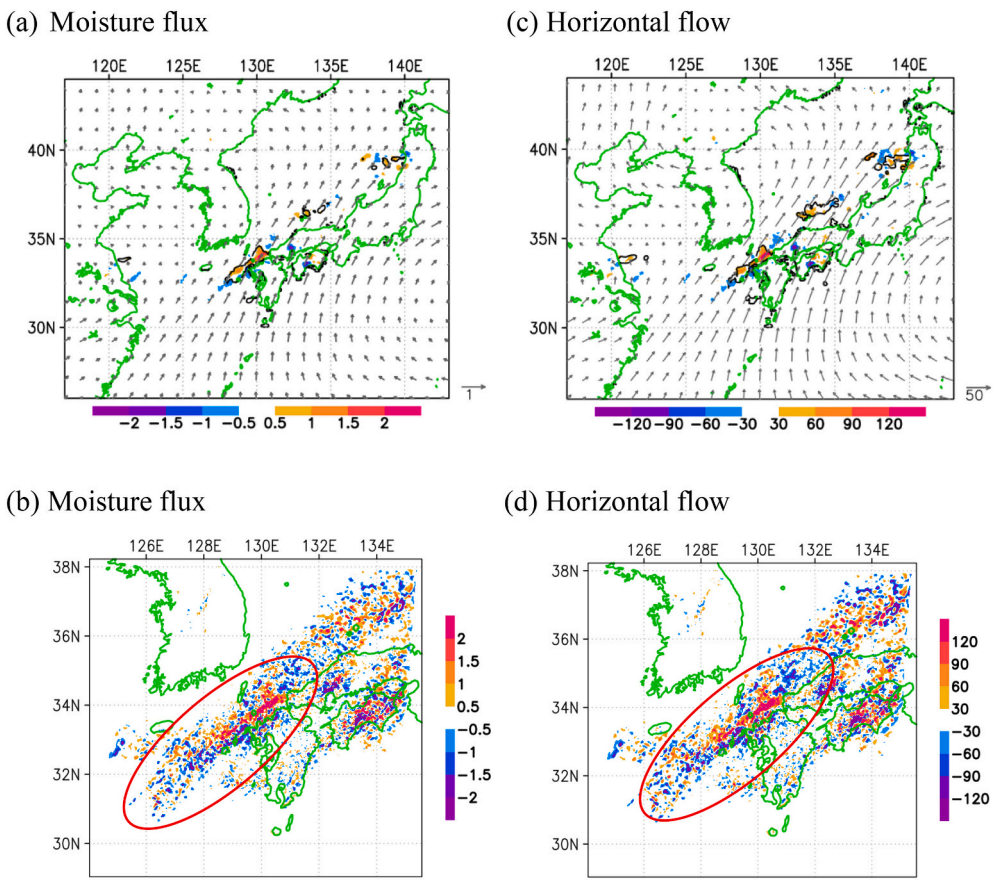

Fig. 9. Distributions of differences (color shading) in the convergence of vertically integrated (a, b) moisture flux and (c, d) horizontal wind from 1000 hPa to 700 hPa on 26 July 2020 between CNTL and CLIM ($\times 10^3$, kg m^{-2} s^{-1}, CNTL − CLIM) in (a, c) Domain 1 and (b, d) Domain 2. The contours indicate the (a) moisture flux convergence (1.0×10^{-3} kg m^{-2} s^{-1}) and (c) wind convergence (50.0×10^{-3} kg m^{-2} s^{-1}) in sea area in CNTL, and the vectors indicate the vertically integrated (a) moisture flux and (c) wind in CNTL ($\times 10^{-3}$, kg m^{-2} m s^{-1}).

mixing ratio rapidly decreased in Fig. 8c). Most of the near-surface parcels (red and blue lines in Fig. 8a) were advected below the 950-hPa altitude. The vapor mixing ratios of the near-surface parcels increased with time before 10–18 h from the rainfall event in Fig. 8c, when the parcels traveled over the East China Sea. Thus the air parcels modified by the sea surface reached the area of abundant water vapor in CNTL. In contrast, water vapor in the air parcels at the lower levels in CLIM (red in Fig. 8d) decreased considerably before the parcels reached the rainfall area in CNTL (before ~5 h): the water vapor in CLIM was removed by condensation over the warmer sea than in CNTL before the moist parcels reached the center of the Tsushima Strait. This implies that the moist air parcels in CNTL reached farther north without losing a large amount of water vapor over the cooler sea than in CLIM. Thus the cool SST anomaly shifted the condensation area northward.

Fig. 9a shows that the lower-level flows advected the water vapor farther northeastward in western Japan below the 700-hPa altitude. The northeastward advection of abundant moisture formed the tongue-shaped moist area (Fig. 5a) over the Japanese main islands (i.e., atmospheric river). The lower-level moisture flux leading to the abundant water vapor and cloud water along the front was advected from the East China Sea (Fig. 6) and converged into the Eastern Channel of the Tsushima Strait, along the horizontal wind convergence area (closed contours of Fig. 9a). Because the horizontal moisture flux and its convergence are similar to those of the horizontal wind (Fig. 9a and c), the lower-level horizontal flow below the 700-Pa altitude converges moisture in the vicinity of the front. In the convergence regions in the Tsushima Strait (closed contours of Fig. 9a and c), the differences in the moisture and wind convergence are positive (CNTL − CLIM >0, red shade in red ovals of Fig. 9b and d): the moisture flux from the southern East China Sea locally increases the water vapor north of Kyushu Island via the enhanced wind convergence. In contrast, the differences in the moisture and wind convergences are negative south of the convergence region in CNTL. This implies that the frontal cloud band is shifted toward Kyushu Island (Fig. 5f) via the lower-level wind convergence (Fig. 9d) for climatological normal SST (CLIM).

In general, convergences of wind and moisture leading to precipitation and clouds in the vicinity of the atmospheric front have often been associated with the surface topography and land/sea contrast. Kyushu's high mountain splits the horizontal flow at 10 m altitude into two along the eastern and western coasts of Kyushu (Fig. 10). The two strong flows converge in the coastal area of northern Kyushu. The east (west) coastal path of the parcels located at 1000 hPa in the moisture convergence region is the dominant flow at 0–12 (12–24) UTC on 26 July 2020 in Fig. 6a. The parcels at 900–700 hPa are transported west of Kyushu (Fig. 6b-d). Such an effect of Kyushu Island's topography on the wind convergence may be an important factor in driving the heavy coastal rain of northern Kyushu in the rainy season when the stationary front is active. The surface moisture convergence is located west of Kyushu Island (purple in red solid oval in Fig. 10a) in CNTL, whereas it is shifted slightly southward to the coastal area of the northern Kyushu in CLIM

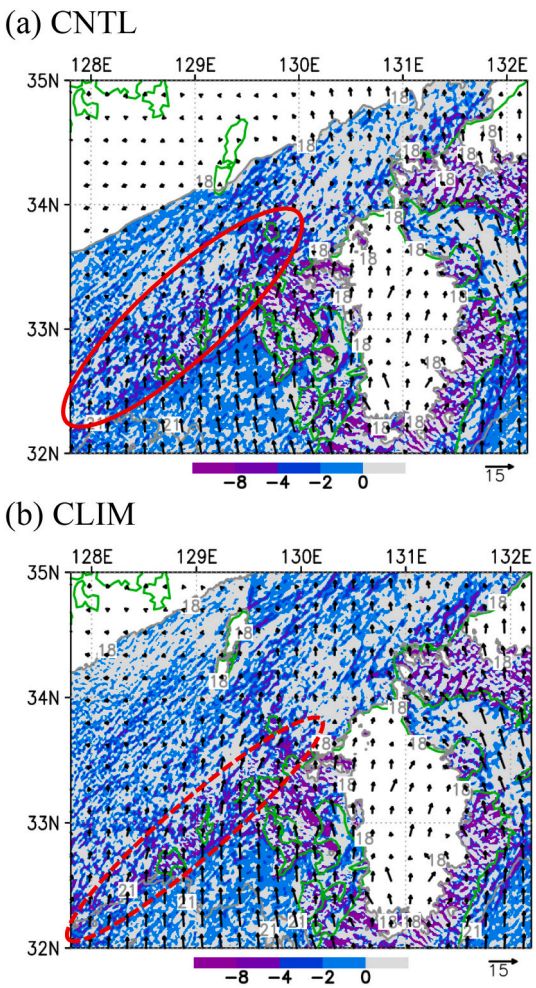

Fig. 10. Distributions of divergence of daily-mean surface moisture fluxes on 26 July 2020 ($\times 10^6$ g kg^{-1} s^{-1}, color shading) in moisture areas where the water vapor mixing at 2 m is higher than 18 g kg^{-1} in Domain 3 for (a) CNTL and (b) CLIM. The gray contours indicate the water vapor mixing at 2 m (g kg^{-1}), the gray shade represents the area of >18 g kg^{-1}, and the vectors show horizontal wind velocity at 10 m (m s^{-1}). The red ovals indicate the convergence regions of the surface moisture. (For interpretation of the references to color in this figure legend, the reader is referred to the web version of this article.)

(Fig. 10b). Because the near-surface water vapor in CLIM is higher than that in CNTL south of the precipitation area, the moist air advected from the south is likely to condense before it extends farther northward. Thus the moisture convergence is confined in a narrower area in CLIM (red dashed oval in Fig. 10b). In contrast, the moisture convergence spreads farther to the north in CNTL (red solid oval in Fig. 10a).

3.4. Distribution of heavy rainfall

Heavy rainfall (>250 mm) is simulated in the Eastern Channel of the Tsushima Strait in CNTL (Fig. 11a) and is similar to the radar precipitation intensity (Fig. 2c). The maximum value of the daily precipitation (273 mm) is higher than that for CLIM (256 mm) in the strait. Compared with CNTL, the precipitation area in CLIM (Fig. 11b) is shifted somewhat southward to the coast of northern Kyushu. This is associated with the southward shift of the convergence area of the moist flow (Figs. 9 and

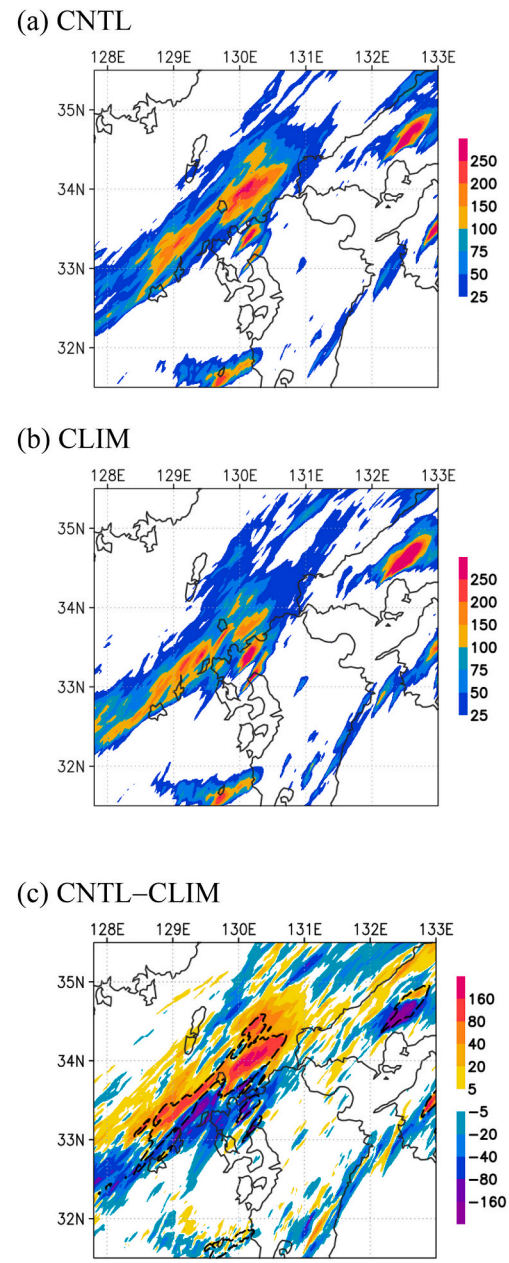

Fig. 11. Distributions of daily precipitation (mm) on 26 July 2020 in (a) CNTL and (b) CLIM, along with (c) the difference in the precipitation between CNTL and CLIM (CNTL − CLIM, color shading). The dashed contours in panel (c) indicate daily precipitation of 100 mm in CNTL.

10), as the water vapors of the moist parcels in CLIM condense before they reach the rainfall area in CNTL (Fig. 8). Thus, the precipitation in CLIM is locally lower than that in CNTL *in* the frontal heavy rain area of CNTL (red in the closed black contour of 100 mm in Fig. 11c). In contrast, the rainfall in CLIM is greater than that in CNTL *south of* the heavy rain area of CNTL (blue areas in Fig. 11c). The large difference in rainfall (CNTL−CLIM) south of the heavy rain area in CNTL is caused by the southward shift of the precipitation and moisture convergence in CLIM. These characteristics of the heavy rain and the difference between CNTL and CLIM are confirmed in all ensemble members of the experiments (Fig. S6).

To remove the remote SST effect over the southern East China and Philippine Seas, the positive SST anomaly over these seas is set to zero in additional experiments using the negative anomaly in the marginal seas (CNTL_N, Fig. 12a); i.e., CNTL_N uses the climatological normal SST in the remote seas and uses the SST for July 2020 (which is lower than the climatological normal) in the marginal seas. In this case, the heavy rain of >100 mm and its difference with CLIM (Fig. 12b) are similar to those in Fig. 11c. Thus the remote SST effect is insignificant, though the moist air is transported from the remote sea areas.

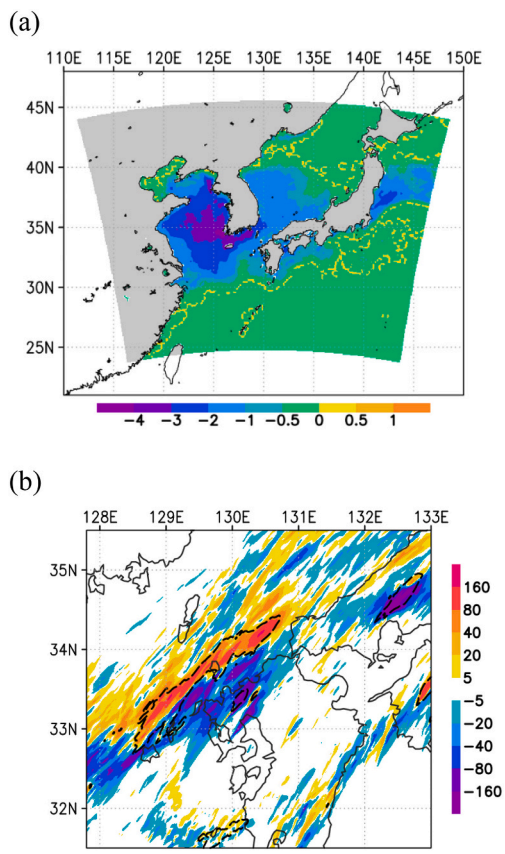

Fig. 12. (a) Negative SST anomaly (K, color shading) used in an additional experiment, CNTL_N. (b) Differences in daily precipitation (mm) between CNTL_N and CLIM (CNTL_N − CLIM, color shading), along with the daily precipitation of 100 mm in CNTL_N (dashed contours).

Table 1
Statistics of area-mean accumulated surface latent heat flux over the area of Fig. 11 (127.8°E-133.0°E, 31.5°N-35.5°N).

	CNTL	CLIM	Remarks
Ensemble average (MJ m^{-2})	1.71	4.04	CNTL−CLIM = −2.33
Standard deviation (MJ m^{-2})	0.06	0.09	
Standard error (MJ m^{-2})	0.02	0.03	CNTL+CLIM = 0.05
SST (K)	298.2	299.5	CNTL−CLIM = −1.32

Table 2
Statistics of daily precipitation averaged over the area of Fig. 11 (127.8°E-133.0°E, 31.5°N-35.5°N).

	CNTL	CLIM	Remarks
Ensemble mean (mm)	22.00	24.04	CNTL−CLIM = −2.04
Standard deviation (mm)	1.03	0.64	
Standard error (mm)	0.36	0.23	CNTL+CLIM = 0.59
SST (K)	298.2	299.5	CNTL−CLIM = −1.32

Table 3
Statistics of maximum daily precipitation in the Eastern Channel of the Tsushima Strait (sea area in 129.0°E-131.0°E, 33.5°N-34.5°N).

	CNTL	CLIM	Remarks
Ensemble average (mm)	289	248	CNTL−CLIM = 41
Standard deviation (mm)	63	16	
Standard error (mm)	22	6	CNTL+CLIM = 28

Table 4
Statistics of maximum daily precipitation over land in the precipitation area (land area in 128.0°E-131.0°E, 32.0°N-35.0°N).

	CNTL	CLIM	Remarks
Ensemble mean (mm)	351	398	CNTL−CLIM = −47
Standard deviation (mm)	56	47	
Standard error (mm)	21	17	CNTL+CLIM = 38

In the rainfall region 31.5°N-35.5°N, 127.8°E-133°E, the area-mean SST and surface latent heat flux in CNTL are lower than those in CLIM (Table 1), averaged for the ensemble experiments (Table S1). Thus, the area-mean daily precipitation in CNTL (22.00 mm) is lower than in CLIM (24.04 mm, Table 2), averaged for the ensemble experiments (Table S2). The precipitation difference (2.04 mm) between the two experiments is statistically significant because it is greater than the sum of the standard errors in CNTL and CLIM (0.59 mm). The cool anomaly in the Tsushima Strait and the adjacent seas reduces the regionally averaged precipitation.

Unlike the area-mean precipitation, the ensemble-mean maximum daily precipitation in CNTL is higher than in CLIM in the Eastern Channel of the Tsushima Strait (Table 3), although some ensemble members show the reverse (Table S3). Thus, we must carefully evaluate the difference in the maximum rainfall intensity between the two SST experiments, as there are large differences among the ensemble members. Because the moist air in CNTL reaches the strait from the southern East China Sea without losing a large amount of moisture to rain, the maxima in the strait in CNTL are much higher than in CLIM for Run −24, −6, and + 12. For the other runs, the difference in the maximum between CLIM and CNTL is small (<25 mm). In the land around the strait, the ensemble-mean maximum precipitation in CLIM is higher than in CNTL (Table 4), except for Run +06 (Table S4). The (relatively warm) climatological normal SST is likely to enhance heavy rainfall in northern Kyushu (on land), associated with the southward shift of the precipitation area in CLIM, because rainfall occurs before the moist air at lower levels (1000 and 900 hPa) reaches the strait in CLIM (Fig. 8b and d).

4. Conclusions

The present work simulated the heavy precipitation on 26 July 2020 in the Tsushima Strait and investigated short-period (24-h) moisture responses to SST. The CNTL (July 2020) experiment showed that, in the Eastern Channel of the Tsushima Strait, daily heavy rainfall of >250 mm occurred along the stationary atmospheric front, northern edge of the tongue-shaped moist area that was extended northeastward by moist flows (i.e., northern edge of the atmospheric river). The moisture leading to the frontal precipitation was transported west of Kyushu from the southern East China Sea (that supplied a large amount of water vapor) and converged by the horizontal lower-level flow in the Eastern Channel of the Tsushima Strait.

Compared with the CLIM experiments using the climatological normal SST, the SST in CNTL is considerably cooler (>1 K) in the Tsushima Strait and slightly warmer (<1 K) in the southern East China Sea. The surface latent heat flux in CNTL was weakened (enhanced) in the cool Tsushima Strait (the warm East China Sea). The water vapor in CNTL decreased north of the atmospheric river and increased in the southern moist area south of 30°N. In the Tsushima Strait area where the

SST and latent heat flux in CNTL are lower than those in CLIM, the area-mean daily precipitation in CNTL is also lower than in CLIM. In contrast to the area means, along the atmospheric front in the Eastern Channel of the Tsushima Strait (~34.0°N, ~130.5°E, north of Kyushu Island), the water-vapor mixing ratio, linear cloud band, and frontal precipitation in CNTL were locally intensified via the remote moisture transport from the southern East China Sea. If this local intensification occurs with climatological SST, the area of heavy precipitation may be shifted from the strait to the heavily populated coastal area with ~million peoples in northern Kyushu. Thus, the intensity and area of heavy rainfalls potentially leading to major natural disasters are sensitive to the SST anomaly from the climatological normal in the marginal seas, where the sea surface conditions vary greatly seasonally.

In this case, the strong surface baroclinicity over the SST front over the Western Channel of the Tsushima Strait and the remote sea-surface conditions over the southern East China Sea do not influence the heavy rainfall over the eastern channel of the strait where the precipitation is located. The large SST anomaly in the vicinity of the Tsushima Strait is a key factor affecting the location of heavy precipitation during the late rainy season in northern Kyushu Island (where heavy rainfall caused by the stationary atmospheric front over the Tsushima Strait often occurs in this season).

CRediT authorship contribution statement

Masaru Yamamoto: Conceptualization, Formal analysis, Investigation, Visualization, Funding acquisition, Writing – original draft, Writing – review & editing.

Declaration of Competing Interest

The authors declare that they have no known competing financial interests or personal relationships that could have appeared to influence the work reported in this paper.

Acknowledgments

The WRF source code (ver. 4.2) was obtained from https://github.com/wrf-model/, the United States Geological Survey land use category data are from http://www2.mmm.ucar.edu/wrf/users/download/get_source.html, the National Centers for Environmental Prediction 6-hourly global final data are from https://rda.ucar.edu/datasets/ds083.3/, and the Japan Meteorological Agency/High resolution Merged satellite and in situ data Sea Surface Temperature data are from http://www.data.jma.go.jp/gmd/goos/data/pub/JMA-product/him_sst_pac_T/. The JMA data were obtained from the JMA website (https://www.jma.go.jp/jma/menu/menureport.html), the Japan Meteorological Business Support Center (http://www.jmbsc.or.jp/), and the Research Institute for Sustainable Humanosphere, Kyoto University (http://database.rish.kyoto-u.ac.jp/arch/jmadata/gpv-original.html). The AMSR2 data were obtained from Remote Sensing Systems (Wentz et al., 2014, https://www.remss.com/missions/amsr/). This study was supported by the Ocean and Atmosphere Research Project of the Research Institute for Applied Mechanics, Kyushu University, Japan (Refinement of Elementary Process Studies on the Ocean and Atmospheric Circulations in the East-Asia Through Basin Scale, and its Application to Environmental Change), and by grants-in-aid from the Ministry of Education, Culture, Sports, Science, and Technology (Japan)/Japan Society for the Promotion of Science (MEXT/JSPS KAKENHI; grant number JP19H05696).

Appendix A. Supplementary data

Supplementary data to this article can be found online at https://doi.org/10.1016/j.atmosres.2022.106336.

References

Cassola, F., Ferrari, F., Mazzino, A., Miglietta, M.M., 2016. The role of the sea on the flash floods events over Liguria (northwestern Italy). Geophys. Res. Lett. 43, 3534–3542. https://doi.org/10.1002/2016GL068265.

Chen, F., Dudhia, J., 2001. Coupling an advanced land surface–hydrology model with the Penn State–NCAR MM5 Modeling System. Part I: Model implementation and sensitivity. Mon. Weather Rev. 129, 569–585. https://doi.org/10.1175/1520-0493(2001)129<0569:CAALSH>2.0.CO;2.

Ferrari, F., Cassola, F., Tuju, P.E., Stocchino, A., Brotto, P., Mazzino, A., 2020. Impact of model resolution and initial/boundary conditions in forecasting flood-causing precipitations. Atmosphere 11, 592. https://doi.org/10.3390/atmos11060592.

Iacono, M.J., Delamere, J.S., Mlawer, E., Shephard, M., Clough, S., Collins, W.D., 2008. Radiative forcing by long-lived greenhouse gases: calculations with the AER radiative transfer models. J. Geophys. Res.-Atmos. 113, D13103. https://doi.org/10.1029/2008JD009944.

Iizuka, S., Nakamura, H., 2019. Sensitivity of midlatitude heavy precipitation to SST: a case study in the Sea of Japan area on 9 August 2013. J. Geophys. Res.-Atmos. 124, 4365–4381. https://doi.org/10.1029/2018JD029503.

Isoguchi, O., Kawamura, H., 2007. Coastal wind jets flowing into the Tsushima Strait and their effect on wind-wave development. J. Atmos. Sci. 64, 564–578. https://doi.org/10.1175/JAS3858.1.

Ito, J., Tsuguchi, H., Hayashi, S., Niino, H., 2021. Idealized high-resolution simulations of a back-building convective system that causes torrential rain. J. Atmos. Sci. 78 (1), 117–132. https://doi.org/10.1175/JAS-D-19-0150.1.

Janjic, Z.I., 1994. The step-mountain eta coordinate model: further developments of the convection, viscous sublayer and turbulence closure schemes. Mon. Weather Rev. 122, 927–945. https://doi.org/10.1175/1520-0493(1994)122<0927:TSMECM>2.0.CO;2.

Janjic, Z.I., 1996. The surface layer in the NCEP Eta Model. In: Preprints, 11th Conference on Numerical Weather Prediction, Norfolk, VA, 19–23 August; Amer. Meteor. Soc., Boston, MA, pp. 354–355.

Janjic, Z.I., 2002. Nonsingular implementation of the Mellor–Yamada level 2.5 scheme in the NCEP Meso model. In: NCEP Office Note, No. 437, p. 61.

Kato, R., Shimose, K., Shimizu, S., 2018. Predictability of precipitation caused by linear precipitation systems during the July 2017 Northern Kyushu heavy rainfall event using a cloud-resolving numerical weather prediction model. J. Disast. Res. 13, 846–859. https://doi.org/10.20965/jdr.2018.p0846.

Kawano, T., Kawamura, R., 2020. Genesis and maintenance processes of a quasi-stationary convective band that produced record-breaking precipitation in Northern Kyushu, Japan on 5 July 2017. J. Meteorol. Soc. Jpn. 98, 673–690. https://doi.org/10.2151/jmsj.2020-033.

Kuwano-Yoshida, A., Minobe, S., Xie, S.-P., 2010. Precipitation Response to the Gulf Stream in an Atmospheric GCM. J. Clim. 23, 3676–3698. https://doi.org/10.1175/2010JCLI3261.1.

Manda, A., Nakamura, H., Asano, N., Iizuka, S., Miyama, T., Moteki, Q., Yoshioka, M.K., Nishii, K., Miyasaka, T., 2014. Impacts of a warming marginal sea on torrential rainfall organized under the Asian summer monsoon. Sci. Rep. 4, 5741. https://doi.org/10.1038/srep05741.

Minobe, S., Kuwano-Yoshida, A., Komori, N., Xie, S.-P., Small, R.J., 2008. Influence of the Gulf Stream on the troposphere. Nature 452, 206–209. https://doi.org/10.1038/nature06690.

Miyama, T., Nonaka, M., Nakamura, H., Kuwano-Yoshida, A., 2012. A striking early-summer event of a convective rainband persistent along the warm Kuroshio in the East China Sea. Tellus A 64, 18962. https://doi.org/10.3402/tellusa.v64i0.18962.

Moteki, Q., Manda, A., 2013. Seasonal migration of the Baiu frontal zone over the East China Sea: sea surface temperature effect. Sci. Online Lett. Atmosph. 9, 19–22. https://doi.org/10.2151/sola.2013-005.

Nayak, S., Takemi, T., 2021. Atmospheric driving mechanisms of extreme precipitation events in July of 2017 and 2018 in western Japan. Dyn. Atmos. Oceans 93, 101186. https://doi.org/10.1016/j.dynatmoce.2020.101186.

Pastor, F., Valiente, J.A., Estrela, M.J., 2015. Sea surface temperature and torrential rains in the Valencia region: modelling the role of recharge areas. Nat. Hazards Earth Syst. Sci. 15, 1677–1693. https://doi.org/10.5194/nhess-15-1677-2015.

Shimada, T., 2010. Structures and seasonal variations of surface winds blowing through the Tsushima Strait. J. Appl. Meteorol. Climatol. 49, 1714–1727. https://doi.org/10.1175/2010JAMC2301.1.

Skamarock, W.C., Klemp, J.B., Dudhia, J., Gill, D.O., Barker, D.M., Duda, M.G., Huang, X.-Y., Wang, W., Powers, J.G., 2008. A description of the Advanced Research WRF Version 3. In: NCAR/TN-475+STR. National Center for Atmospheric Research, p. 126.

Stunder, B.J., 1996. An assessment of the quality of forecast trajectories. J. Appl. Meteorol. 35, 1319–1331. https://doi.org/10.1175/1520-0450(1996)035<1319:AAOTQO>2.0.CO;2.

Takikawa, T., Yoon, J., Cho, K., 2005. The Tsushima warm current through Tsushima Straits estimated from ferryboat ADCP Data. J. Phys. Oceanogr. 35, 1154–1168. https://doi.org/10.1175/JPO2742.1.

Thompson, G., Field, P.R., Rasmussen, R.M., Hall, W.D., 2008. Explicit forecasts of winter precipitation using an improved bulk microphysics scheme. Part II: Implementation of a new snow parameterization. Mon. Weather Rev. 136, 5095–5115. https://doi.org/10.1175/2008MWR2387.1.

Tiedtke, M., 1989. A comprehensive mass flux scheme for cumulus parameterization in largescale models. Mon. Weather Rev. 117, 1779–1800. https://doi.org/10.1175/1520-0493(1989)117<1779:ACMFSF>2.0.CO;2.

Toy, M.D., Johnson, R.H., 2014. The influence of an SST front on a heavy rainfall event over coastal Taiwan during TiMREX. J. Atmos. Sci. 71, 3223–3249. https://doi.org/10.1175/JAS-D-13-0338.1.

Wentz, F.J., Meissner, T., Gentemann, C., Hilburn, K.A., Scott, J., 2014. Remote Sensing Systems GCOM-W1 AMSR2 Daily Environmental Suite on 0.25 deg grid, Version 8.2. Remote Sensing Systems, Santa Rosa, CA. available online at. https://www.remss.com/missions/amsr/.

Yamamoto, M., 2014. Meteorological impacts of sea-surface temperature associated with the humid airflow from Tropical Cyclone Talas (2011). Ann. Geophys. 32, 841–857. https://doi.org/10.5194/angeo-32-841-2014.

Yamamoto, M., 2018. Migration of contact binary cyclones and atmospheric river: case of explosive extratropical cyclones in East Asia on December 16, 2014. Dyn. Atmos. Oceans 83, 17–40. https://doi.org/10.1016/j.dynatmoce.2018.05.003.

Yamamoto, M., 2020. Ensemble simulations of the influence of regionally warm sea surface on moisture and rainfall in Tsushima Strait during August 2013. Atmos. Res. 238, 104876. https://doi.org/10.1016/j.atmosres.2020.104876.

Zhao, N., Manda, A., Guo, X., Kikuchi, K., Nasuno, T., Nakano, M., et al., 2021. A Lagrangian view of moisture transport related to the heavy rainfall of July 2020 in Japan: Importance of the moistening over the subtropical regions. Geophys. Res. Lett. 48, e2020GL091441 https://doi.org/10.1029/2020GL091441.